

GEOMETRY-AWARE UNCERTAINTY QUANTIFICATION VIA CONFORMAL PREDICTION ON MANIFOLDS

Marzieh Amiri Shahbazi

Rochester Institute of Technology
ma7684@rit.edu

Ali Baheri

Rochester Institute of Technology
akbeme@rit.edu

ABSTRACT

Conformal prediction provides distribution-free coverage guarantees for regression; yet existing methods assume Euclidean output spaces and produce prediction regions that are poorly calibrated when responses lie on Riemannian manifolds. We propose *adaptive geodesic conformal prediction*, a framework that replaces Euclidean residuals with geodesic nonconformity scores and normalizes them by a cross-validated difficulty estimator to handle heteroscedastic noise. The resulting prediction regions, geodesic caps on the sphere, have position-independent area and adapt their size to local prediction difficulty, yielding substantially more uniform conditional coverage than non-adaptive alternatives. In a synthetic sphere experiment with strong heteroscedasticity and a real-world geomagnetic field forecasting task derived from IGRF-14 satellite data, the adaptive method markedly reduces conditional coverage variability and raises worst-case coverage much closer to the nominal level, while coordinate-based baselines waste a large fraction of coverage area due to chart distortion.

1 INTRODUCTION

Prediction problems with manifold-valued responses arise throughout the sciences: geomagnetic field directions lie on the unit sphere (Alken et al., 2021), protein backbone dihedral angles reside on the flat torus (Ramachandran et al., 1963), spacecraft orientations belong to the rotation group (Peretroukhin et al., 2020), and brain connectivity patterns take values in the space of symmetric positive definite matrices (Yuan et al., 2012). Point prediction for such data has advanced considerably (Petersen & Müller, 2019; Lin et al., 2017; Fletcher, 2013), yet a fundamental question remains open: *how should we quantify uncertainty for manifold-valued predictions?* Conformal prediction (CP) provides a compelling answer in the Euclidean setting. Given exchangeable data and any base predictor, split CP constructs prediction regions with finite-sample, distribution-free coverage guarantees (Vovk et al., 2005; Lei et al., 2018), along with recent extensions to covariate shift (Tibshirani et al., 2019), improved conditional coverage (Romano et al., 2019), and non-exchangeable data (Barber et al., 2023). However, applying CP to manifold-valued responses introduces two challenges. *First, the geometry of the output space matters.* Standard CP uses Euclidean residuals as nonconformity scores, producing hypercubes or balls. On a curved manifold, coordinate-based distances inherit chart distortions that inflate prediction regions. On the sphere, for instance, a coordinate rectangle of fixed half-width has an area that varies with latitude, vanishing near the poles and maximal at the equator, while a geodesic cap of the same radius has a constant area everywhere. Ignoring this distinction wastes a substantial fraction of coverage area in our experiments. *Second, heteroscedasticity is the rule, not the exception.* In geomagnetic forecasting, secular variation rates differ by an order of magnitude between polar and equatorial regions. A constant-width prediction region will over-cover easy regions and under-cover hard ones: in our geomagnetic experiment, the non-adaptive geodesic method achieves worst-case conditional coverage well below the nominal level. Normalizing residuals by a local difficulty estimate is the standard Euclidean remedy (Lei et al., 2018; Romano et al., 2019); its manifold analog requires geodesic distances and geometry-aware difficulty estimation.

Related work. CP on manifolds has received limited attention. Kuleshov et al. (2018) constructs prediction regions in a learned embedding rather than on the output manifold. Messoudi et al. (2021; 2022) addresses multi-target regression with copula-based and ellipsoidal regions in Euclidean space. More broadly, several recent works have extended CP beyond the standard i.i.d. Euclidean

setting: [Amiri Shahbazi et al. \(2026\)](#) combines group-aware conformal calibration with Bayesian posterior uncertainties for hierarchical healthcare data; [Baheri & Amiri Shahbazi \(2025\)](#) intersects scale-specific prediction sets to improve efficiency in multi-resolution problems; and [Millard et al. \(2025\)](#) lifts split conformal guaranties to infinite-dimensional function spaces via neural operators. These extensions address hierarchical, multi-scale, and functional structures in the data but do not account for the intrinsic geometry of the output space, which is the focus of our work.

Contributions: We propose *adaptive geodesic conformal prediction* for manifold-valued regression, combining intrinsic geometry with locally adaptive calibration.

1. **Geometry-aware conformal regions.** We construct conformal prediction sets using intrinsic (geodesic) distances, producing regions that respect the manifold geometry (e.g., spherical caps with location-independent area), unlike coordinate-based sets that suffer from chart distortion.
2. **Locally adaptive calibration without breaking coverage.** We incorporate a covariate-dependent difficulty estimate to adapt region size across easy and hard inputs, trained only on the proper training data (via cross-validation) so that the split-conformal coverage guaranty is preserved.
3. **Empirical validation.** On a controlled synthetic benchmark and an IGRF-based geomagnetic direction forecasting task, the method reduces conditional coverage variability and improves worst-case coverage while maintaining valid marginal coverage and competitive region size.

2 METHOD

We consider the manifold-valued regression setting: covariates $X \in \mathcal{X} \subseteq \mathbb{R}^p$ are paired with responses Y on a complete Riemannian manifold (\mathcal{M}, g) equipped with geodesic distance d_{geo} . The goal is to construct a prediction region $\mathcal{C}(X) \subseteq \mathcal{M}$ satisfying $\mathbb{P}(Y_{n+1} \in \mathcal{C}(X_{n+1})) \geq 1 - \alpha$ for a user-specified level α , while keeping the region as small as possible. Beyond this marginal guaranty, we seek regions whose conditional coverage $\mathbb{P}(Y \in \mathcal{C}(X) \mid X = x) \approx 1 - \alpha$ is uniform over x , rather than over-covering easy regions and under-covering hard ones.

We instantiate the framework on two manifolds. The unit sphere $\mathbb{S}^2 = \{y \in \mathbb{R}^3 : \|y\| = 1\}$ arises in geomagnetic and directional data; the geodesic distance is $d_{\text{geo}}(u, v) = \arccos(\langle u, v \rangle)$, and the geodesic ball (spherical cap) of radius r has an area $2\pi(1 - \cos r)$, independent of position. The flat torus $\mathbb{T}^2 = [-\pi, \pi]^2$ arises in protein backbone dihedral angles; the geodesic distance is $d_{\text{geo}}(u, v) = \sqrt{d_{\text{o}}(u_1, v_1)^2 + d_{\text{o}}(u_2, v_2)^2}$, where d_{o} denotes circular distance, and the geodesic disk of radius r has an area πr^2 .

2.1 CONFORMAL PREDICTION WITH GEODESIC SCORES

We adopt the split conformal framework ([Vovk et al., 2005](#); [Lei et al., 2018](#)), partitioning the data into a training set \mathcal{D}_{tr} , a calibration set \mathcal{D}_{cal} , and a test set \mathcal{D}_{te} . The training set is used to fit a point predictor $\hat{y} : \mathcal{X} \rightarrow \mathcal{M}$ and a difficulty estimator $\hat{\sigma} : \mathcal{X} \rightarrow \mathbb{R}_+$; the calibration set determines the prediction region width. Specifically, we compute nonconformity scores $s(X_i, Y_i)$ on each calibration point, take the conformal quantile \hat{q}_α at level $\lceil (1 - \alpha)(n_{\text{cal}} + 1) \rceil / n_{\text{cal}}$, and define the prediction region as $\mathcal{C}(x) = \{y \in \mathcal{M} : s(x, y) \leq \hat{q}_\alpha\}$. By the exchangeability of the calibration and test data (conditioned on \mathcal{D}_{tr}), this guarantees $\mathbb{P}(Y_{n+1} \in \mathcal{C}(X_{n+1})) \geq 1 - \alpha$ regardless of the score function, the distribution, or the manifold ([Vovk et al., 2005](#)). Since coverage holds for *any* score, the choice of s affects only the efficiency and conditional coverage of the resulting regions, a freedom we exploit by designing geometry-aware scores.

We compare three nonconformity scores. Our proposed **adaptive geodesic** score divides the geodesic residual by a local difficulty estimate,

$$s_{\text{adapt}}(x, y) = d_{\text{geo}}(\hat{y}(x), y) / \hat{\sigma}(x), \quad (1)$$

producing a geodesic ball $\mathcal{C}(x) = B_{\text{geo}}(\hat{y}(x), \hat{q}_\alpha \cdot \hat{\sigma}(x))$ whose radius shrinks where the model is confident and expands where prediction is difficult. This is the manifold analog of the locally-adaptive score of [Lei et al. \(2018\)](#) and [Romano et al. \(2019\)](#), replacing the Euclidean residual with a geodesic

distance. The **standard geodesic** score uses the unnormalized distance $s_{\text{geo}}(x, y) = d_{\text{geo}}(\hat{y}(x), y)$, yielding a constant-radius ball that respects the geometry but ignores heteroscedasticity. The **naive coordinate** score applies an L^∞ distance in a coordinate chart, spherical coordinates for \mathbb{S}^2 , and dihedral angles for \mathbb{T}^2 , producing axis-aligned rectangles in the chart. This is the most direct Euclidean generalization, ignoring both geometry and heteroscedasticity.

The geometric distinction between these scores is consequential. On \mathbb{S}^2 , both geodesic scores produce spherical caps with position-independent areas, while the coordinate rectangle has an area proportional to $\sin \theta$, vanishing near the poles and maximal at the equator. A fixed coordinate width, therefore, wastes area in equatorial regions while providing insufficient coverage near the poles; the L^∞ norm also treats the θ and φ directions identically, despite the metric weighting φ by $\sin \theta$. In our IGRF-14 experiment, this distortion causes the naive method to use substantially more total area than the geodesic methods at identical marginal coverage. On \mathbb{T}^2 , chart distortion does not apply (the metric is flat), but geodesic disks are still more efficient than coordinate squares by the constant $\pi/4$: a circle inscribed in a square covers only about 79% of the square's area. The adaptive score is the only one whose region size varies across test points, which, in heteroscedastic settings, both reduces mean area and improves conditional coverage uniformity. The base predictor \hat{y} can be any model producing manifold-valued outputs; the coverage guaranty is agnostic to this choice. We use k -nearest-neighbor regressors with manifold-appropriate aggregation: on \mathbb{S}^2 , the extrinsic mean (Euclidean average of neighbors projected onto the sphere); on \mathbb{T}^2 , the circular mean computed independently on each angular coordinate to avoid wraparound artifacts.

Difficulty Estimation and Diagnosis. The adaptive score equation 1 requires a difficulty estimator $\hat{\sigma}(x)$ that predicts the magnitude of the geodesic residual from covariates alone. Critically, $\hat{\sigma}$ must be trained without access to the calibration set so that calibration scores remain exchangeable and the coverage guaranty holds. We estimate $\hat{\sigma}$ using a two-stage procedure applied solely to \mathcal{D}_{tr} . In the first stage, we compute cross-validated residuals: the training set is partitioned into five folds, and for each fold k the base model is refit on the remaining folds to produce geodesic residuals $e_i = d_{\text{geo}}(\hat{y}^{(-k)}(X_i), Y_i)$ on the held-out points. Because each e_i comes from a model that did not see (X_i, Y_i) , these residuals are approximately unbiased. In the second stage, we fit a k -nearest-neighbor regressor to predict residuals from covariates: $\hat{\sigma}(x) = \frac{1}{k_\sigma} \sum_{j \in \mathcal{N}(x)} e_j$ with $k_\sigma = 20$ neighbors, clipped below at a small $\epsilon > 0$ to prevent division by zero. Since $\hat{\sigma}$ is fixed before any calibration scores are computed, exchangeability is preserved and the coverage guaranty continues to hold.

The effectiveness of the adaptive method depends on how well $\hat{\sigma}$ predicts actual prediction difficulty. We measure this via the Pearson correlation $r = \text{Corr}(\hat{\sigma}(X), d_{\text{geo}}(\hat{y}(X), Y))$ on held-out data. When this correlation is high, the normalization in equation 1 effectively standardizes scores across difficulty levels, yielding uniform conditional coverage. When the correlation is near zero, normalization adds noise, and the standard geodesic score is preferable. We propose this correlation as a practical deployment diagnostic: compute it on a validation set before choosing between adaptive and non-adaptive methods.

Conditional Coverage Evaluation. The marginal guaranty is an average over the distribution of X ; a method can satisfy it while dramatically over-covering easy regions and under-covering hard ones. Although exact conditional coverage is unachievable in finite samples without distributional assumptions, approximate conditional coverage can be evaluated empirically. We bin test points into six equal-frequency groups by estimated difficulty $\hat{\sigma}(x)$ and compute bin-level coverage Cov_b . Two summary statistics capture uniformity: the standard deviation across bins (the lower, the better) and the worst-case bin coverage (the higher, the better). The adaptive score pursues uniformity by standardizing residuals: when $\hat{\sigma}(x)$ is proportional to the expected geodesic error at x , a single conformal quantile controls coverage at all difficulty levels simultaneously.

The complete procedure is summarized below. The dominant computational costs are fitting the base model, the five-fold cross-validation for difficulty estimation, and computing geodesic distances, all of which are linear in sample size per test point, with geodesic distances requiring only an inner product and an arccos on \mathbb{S}^2 .

Algorithm 1 Adaptive Geodesic Conformal Prediction on \mathcal{M}

Require: Data $\{(X_i, Y_i)\}_{i=1}^n$, manifold $(\mathcal{M}, d_{\text{geo}})$, level α , split ratios
Ensure: Prediction regions $\{\mathcal{C}(X_i)\}_{i \in \mathcal{D}_{\text{te}}}$ with coverage $\geq 1 - \alpha$

Training (uses \mathcal{D}_{tr} only):

- 1: Fit base predictor \hat{y} on \mathcal{D}_{tr}
- 2: Compute CV residuals: $e_i = d_{\text{geo}}(\hat{y}^{(-k)}(X_i), Y_i)$ for each $i \in \mathcal{D}_{\text{tr}}$
- 3: Fit difficulty estimator $\hat{\sigma}$ by regressing e_i on X_i

Calibration (uses \mathcal{D}_{cal} only):

- 4: Compute scores $s_i = d_{\text{geo}}(\hat{y}(X_i), Y_i) / \max(\hat{\sigma}(X_i), \epsilon)$ for each $i \in \mathcal{D}_{\text{cal}}$
- 5: $\hat{q}_\alpha \leftarrow$ conformal quantile of $\{s_i\}$ at level $\lceil (1 - \alpha)(n_{\text{cal}} + 1) \rceil / n_{\text{cal}}$

Prediction:

- 6: **for** each test point x **do**
- 7: $\mathcal{C}(x) \leftarrow B_{\text{geo}}(\hat{y}(x), \hat{q}_\alpha \cdot \max(\hat{\sigma}(x), \epsilon))$
- 8: **end for**

We note two limitations of the current framework. First, the marginal guaranty requires exchangeability, which may be violated in streaming or temporally ordered settings; extensions using non-exchangeable conformal prediction (Barber et al., 2023) are a natural direction. Second, prediction regions are isotropic geodesic balls; on manifolds where prediction error is anisotropic, ellipsoidal or kernel-shaped regions could be more efficient, though constructing such regions with exact conformal coverage remains open.

3 RIEMANNIAN GEOMETRY PRELIMINARIES

Our experiments focus on the unit two-sphere \mathbb{S}^2 , the simplest closed Riemannian manifold with nonzero curvature. This section summarizes the geometric facts used in our construction and analysis. The central point is that curvature induces unavoidable distortion in coordinate charts, so prediction regions defined in coordinates do not correspond to uniform intrinsic (geodesic) regions on the manifold. In contrast, geometry-aware regions defined by the geodesic distance have consistent intrinsic size and admit clean efficiency comparisons.

3.1 THE 2-SPHERE \mathbb{S}^2

The unit sphere $\mathbb{S}^2 = \{y \in \mathbb{R}^3 : \|y\| = 1\}$ carries the round metric inherited from \mathbb{R}^3 . For $u, v \in \mathbb{S}^2$, the geodesic distance is the great-circle distance

$$d_{\text{geo}}(u, v) = \arccos(\langle u, v \rangle) \in [0, \pi]. \quad (2)$$

The geodesic ball (spherical cap) of radius r centered at μ is $B_{\text{geo}}(\mu, r) = \{y \in \mathbb{S}^2 : d_{\text{geo}}(\mu, y) \leq r\}$, and its Riemannian area is

$$\text{Area}(B_{\text{geo}}(\mu, r)) = 2\pi(1 - \cos r) \quad (\text{steradians}). \quad (3)$$

Crucially, this area depends only on r and not on μ , reflecting the homogeneity of \mathbb{S}^2 . As a result, calibrating a conformal quantile \hat{q}_α using geodesic residuals yields prediction regions whose intrinsic size is comparable across locations on the sphere.

Coordinate charts and distortion. In standard spherical coordinates (θ, φ) with colatitude $\theta \in [0, \pi]$ and azimuth $\varphi \in [-\pi, \pi]$, the metric is $ds^2 = d\theta^2 + \sin^2 \theta d\varphi^2$. An L^∞ -ball of half-width δ in these coordinates defines the rectangle $\{(\theta', \varphi') : |\theta' - \theta| \leq \delta, |\varphi' - \varphi| \leq \delta\}$, whose area is

$$\text{Area}_{\text{naive}}(\delta, \theta) = 2\delta |\cos(\theta - \delta) - \cos(\theta + \delta)|. \quad (4)$$

Unlike equation 3, this quantity depends on the location θ . The dependence comes from the $\sin \theta$ factor in the metric: near the poles ($\theta \approx 0$ or π), the azimuthal direction is metrically compressed, so a fixed coordinate half-width δ corresponds to a very small intrinsic (geodesic) width in φ . Consequently, fixed-width coordinate rectangles can become intrinsically too narrow near the poles and tend to under-cover there. Conversely, if one attempts to enforce an approximately fixed intrinsic radius using a coordinate rectangle, the required longitude half-width must scale like $\delta_\varphi \propto 1 / \sin \theta$, which can make such rectangles overly conservative (and sometimes substantially larger in area than geodesic caps) away from the poles. This nonuniformity is a geometric manifestation of positive curvature: no single global coordinate chart can be everywhere isometric to \mathbb{R}^2 on \mathbb{S}^2 .

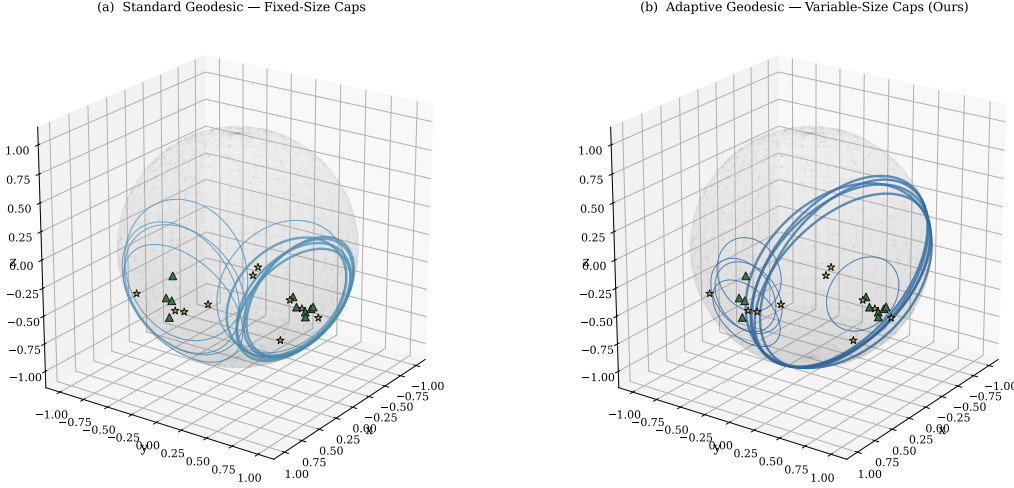


Figure 1: Standard geodesic CP uses fixed-radius caps for every test point (left), while adaptive geodesic CP varies cap size by local difficulty (right).

4 EXPERIMENTAL SETUP

We compare three conformal prediction methods on \mathbb{S}^2 : **Adaptive Geodesic** (proposed), which uses the normalized score $s(x, y) = d_{\text{geo}}(\hat{y}(x), y)/\hat{\sigma}(x)$ and produces geodesic caps of variable radius $r(x) = \hat{q}_\alpha \cdot \hat{\sigma}(x)$; **Standard Geodesic**, which uses $s(x, y) = d_{\text{geo}}(\hat{y}(x), y)$ and produces constant-radius caps; and **Naive Coordinate**, which uses the L^∞ distance in spherical coordinates (θ, φ) , producing axis-aligned rectangles. All three satisfy the marginal coverage guaranty $\mathbb{P}(Y_{n+1} \in \mathcal{C}(X_{n+1})) \geq 1 - \alpha$ by construction; they differ in conditional coverage and efficiency. The difficulty estimator $\hat{\sigma}(x)$ is trained via 5-fold cross-validation on the training set alone to preserve exchangeability. The base predictor is a k -NN regressor ($k = 20$) with extrinsic mean projection onto \mathbb{S}^2 . We evaluate marginal coverage, mean region area (steradians), conditional coverage standard deviation across 6 equal-frequency difficulty bins, and worst-case bin-level coverage.

Case Study 1: Synthetic Sphere with Controlled Heteroscedasticity

We sample $n = 1,200$ points with covariates $x \in [-3, 3]^2$ and responses $Y \sim \text{vMF}(\mu(x), \kappa(x))$, where the concentration $\kappa(x) = 3 + 147 \exp(-\|x\|^2/4)$ varies $50\times$ from boundary (highly dispersed, $\sim 33^\circ$ error) to center (tightly concentrated, $\sim 4.7^\circ$ error). Table 1 reports 300-trial results at $\alpha = 0.10$. All methods achieve valid marginal coverage. The adaptive geodesic method reduces the conditional coverage standard deviation by 19% (0.042 vs. 0.052) and raises the worst-case coverage from 0.814 to 0.839. The naive coordinate method wastes 26% more area than the geodesic methods due to metric distortion near the poles.

Table 1: Synthetic \mathbb{S}^2 : 300 trials, $\alpha = 0.10$, $n = 1,200$, $50\times$ heteroscedasticity.

Method	Marg. Cov.	Area (sr)	Cond. Std. \downarrow	Worst Cov. \uparrow
Adaptive Geodesic	0.906 ± 0.020	1.865	0.042	0.839
Standard Geodesic	0.904 ± 0.019	1.885	0.052	0.814
Naive Coordinate	0.904 ± 0.019	2.376	0.067	0.784

Figure 3 confirms the mechanism. Panel (a) bins test points by estimated difficulty: the standard and naive methods over-cover easy regions (> 0.99) while under-covering hard regions (< 0.70); the adaptive method maintains coverage near 0.90 across all difficulty levels. Panel (b) bins by the true vMF concentration $\kappa(x)$, which directly controls dispersion: at low κ (hard, dispersed targets), both non-adaptive methods drop well below the target, while the adaptive method stays flat.

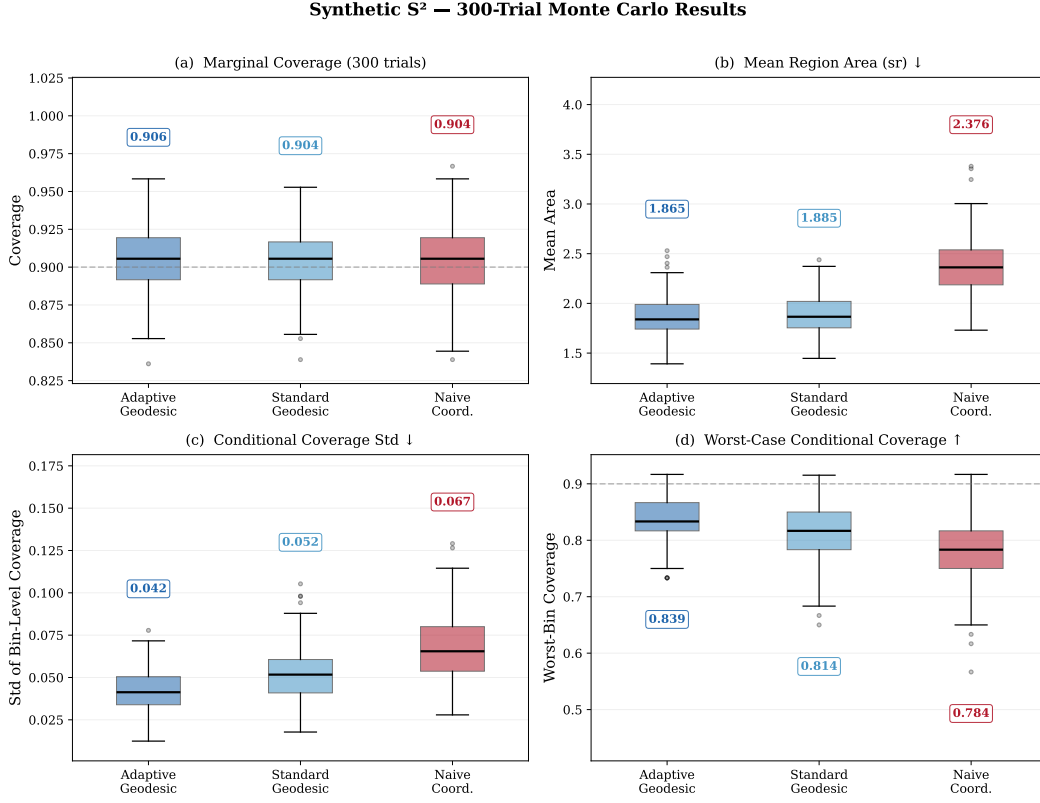


Figure 2: 300-trial Monte Carlo distributions. (a) Valid marginal coverage for all methods. (b) Naive coordinate wastes 26% more area. (c) Adaptive method achieves lowest conditional coverage variance. (d) Adaptive worst-case coverage stays closest to the 0.90 target.

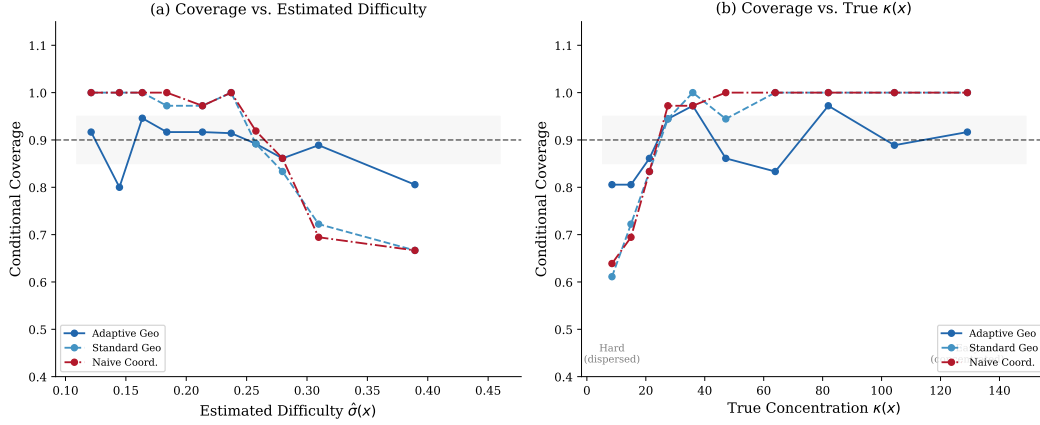


Figure 3: Conditional coverage vs. estimated difficulty $\hat{\sigma}(x)$ (left) and true vMF concentration $\kappa(x)$ (right). The adaptive method stays flat near 0.90 across all difficulty levels; the standard and naive methods over-cover easy (high- κ) regions while under-covering hard (low- κ) regions.

Case Study 2: IGRF-14 Geomagnetic Field Forecasting

We construct a temporal forecasting task from the International Geomagnetic Reference Field Alken et al. (2021), whose spherical harmonic coefficients are derived from the ESA Swarm satellite constellation. At 352 surface locations (52 INTERMAGNET observatories + 300 random sites), we

compute the geomagnetic field unit vector $\hat{\mathbf{B}}(x, t) \in \mathbb{S}^2$ at 38 semi-annual epochs (2005–2023) and predict $\hat{\mathbf{B}}(x, t + 1 \text{ yr})$ from (lat, lon, $\hat{\mathbf{B}}(x, t), t$), yielding 3,000 subsampled forecast pairs.

No synthetic noise is added. Prediction residuals arise from the k -NN model’s inability to extrapolate real secular variation. This variation is inherently heteroscedastic: near the South Atlantic Anomaly and magnetic equator, the field evolves far faster than near the poles, with a ratio of up to $274 \times$ between the fastest- and slowest-changing locations (Figure 4b). Table 2 presents 100-trial results. The difficulty estimator achieves Pearson $r = 0.516$ ($p < 10^{-123}$) with actual residuals, confirming that $\hat{\sigma}(x)$ captures the spatial pattern of the secular variation rate. The adaptive method reduces the conditional coverage standard deviation by 71% (0.031 vs. 0.107) and raises the worst-case coverage from 0.689 to 0.855. The standard geodesic method severely under-covers equatorial regions (worst-bin < 0.70), exactly where reliable uncertainty quantification is most needed.

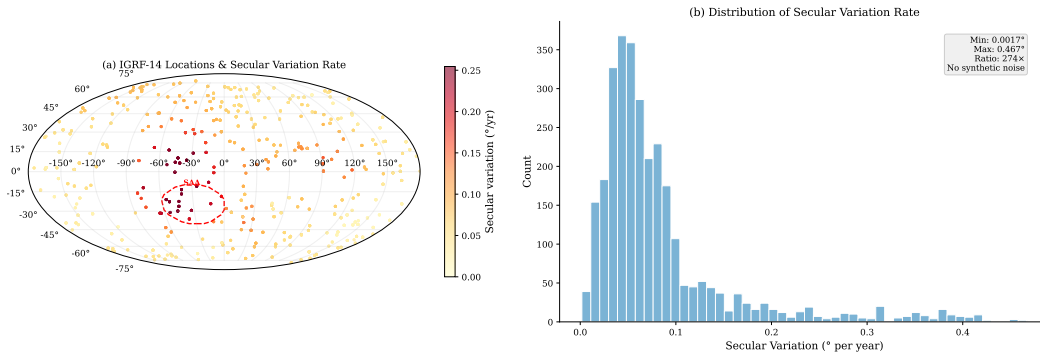


Figure 4: (a) Secular variation rate across the globe. Equatorial and South Atlantic regions exhibit the fastest field evolution, creating natural heteroscedasticity. (b) Distribution of secular variation rates, spanning a $274 \times$ range.

Across both experiments, the adaptive geodesic method consistently achieves the best conditional coverage uniformity and worst-case coverage while maintaining valid marginal coverage. Two distinct mechanisms drive the improvement: (i) *adaptivity*—normalizing by $\hat{\sigma}(x)$ standardizes conformity scores across difficulty levels, yielding uniform conditional coverage when the estimator is informative ($r > 0.3$); and (ii) *geometry*—geodesic caps have position-independent area on \mathbb{S}^2 , whereas coordinate rectangles waste area due to metric distortion. The $\hat{\sigma}$ residual correlation r serves as a practical diagnostic: on IGRF-14, $r = 0.516$ translates to a 71% reduction in conditional coverage standard deviation. We recommend computing this diagnostic on a validation set before deployment; if $r < 0.15$, the standard geodesic method is preferable.

Table 2: IGRF-14 geomagnetic forecasting (\mathbb{S}^2): 100 trials, $\alpha = 0.10$, $n = 3,000$. Difficulty estimator: $r(\hat{\sigma}, \text{residual}) = 0.516$.

Method	Marg. Cov.	Area (sr)	Cond. Std \downarrow	Worst Cov. \uparrow
Adaptive Geodesic	0.902 ± 0.013	0.038	0.031	0.855
Standard Geodesic	0.902 ± 0.013	0.039	0.107	0.689
Naive Coordinate	0.903 ± 0.015	0.046	0.060	0.805
<i>Wilcoxon signed-rank (Adaptive vs. Standard):</i>			$p < 4 \times 10^{-18}$	$p < 4 \times 10^{-18}$

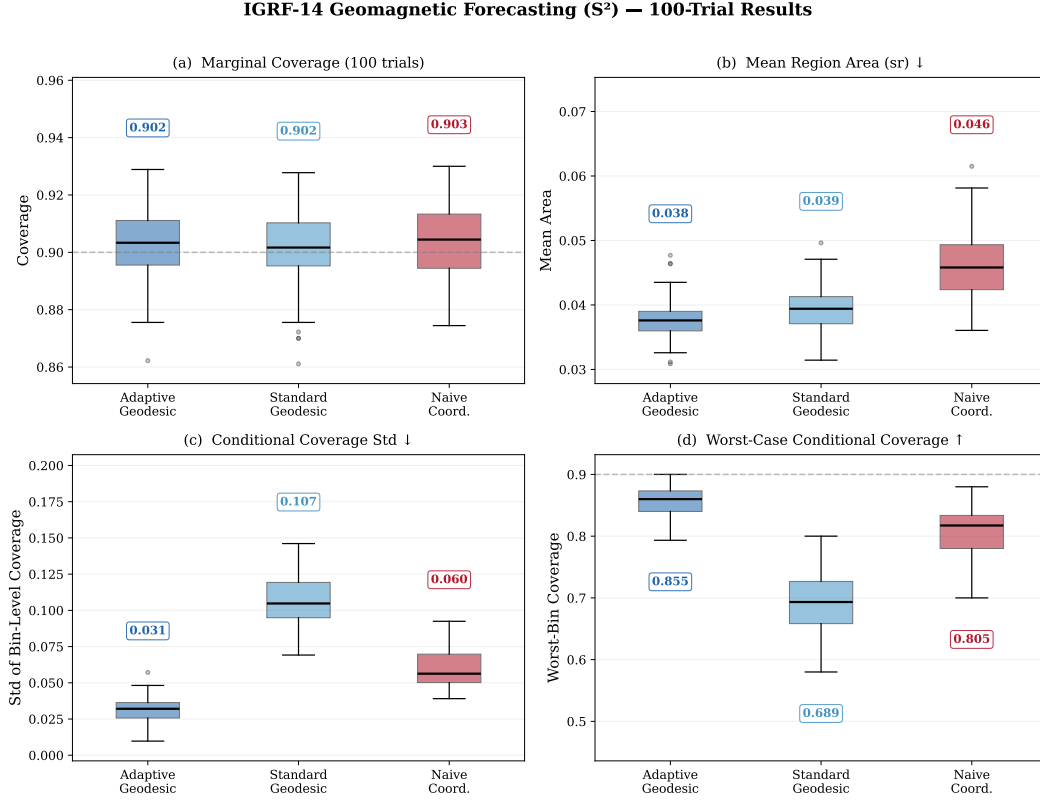


Figure 5: IGRF-14: 100-trial results. The adaptive method achieves $3.5 \times$ lower conditional coverage standard deviation and raises worst-case coverage by 0.166.

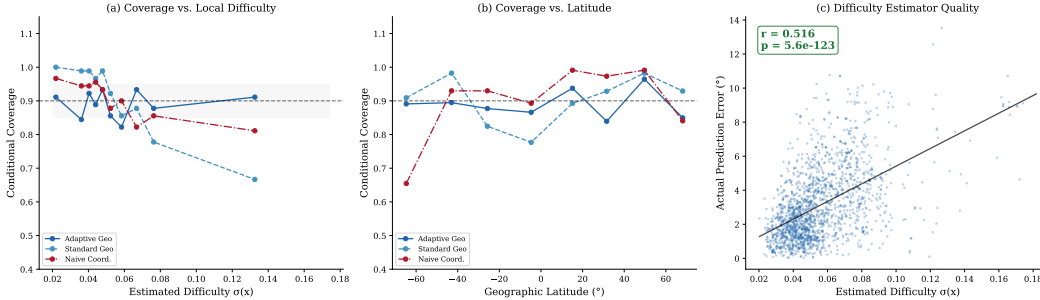


Figure 6: (a) Conditional coverage vs. estimated difficulty: the standard geodesic drops below 0.60 for the hardest bin while the adaptive method stays near 0.90. (b) Coverage vs. geographic latitude: the standard method under-covers equatorial latitudes where secular variation is fastest. (c) Difficulty estimator diagnostic ($r = 0.516, p < 10^{-123}$).

CONCLUSION

We introduced adaptive geodesic conformal prediction, a framework that combines geometry-aware nonconformity scores with local difficulty estimation to produce distribution-free prediction regions on Riemannian manifolds. Two complementary mechanisms drive the improvement over standard baselines: geodesic scores yield prediction regions with position-independent area, eliminating the chart distortion that causes coordinate-based methods to waste coverage; and normalizing by a cross-validated difficulty estimator adapts region size to local uncertainty, substantially equalizing conditional coverage across difficulty levels. On both a synthetic sphere task with $50 \times$ heteroscedas-

ticity and a real geomagnetic forecasting task derived from IGRF-14 satellite data, the adaptive method achieves the most uniform conditional coverage and the highest worst-case bin coverage, with all improvements statistically significant. Extensions include adapting the framework to streaming settings via non-exchangeable conformal prediction and generalizing beyond isotropic geodesic caps to anisotropic prediction regions that could further tighten coverage on manifolds where prediction error is direction-dependent.

REFERENCES

P. Alken, E. Thébault, C. D. Beggan, H. Amit, J. Aubert, J. Baerenzung, T. N. Bondar, W. J. Brown, S. Califf, A. Chambodut, et al. International Geomagnetic Reference Field: the thirteenth generation. *Earth, Planets and Space*, 73:49, 2021. doi: 10.1186/s40623-020-01288-x.

Marzieh Amiri Shahbazi, Ali Baheri, and Nasibeh Azadeh-Fard. A hierarchical conformal framework for uncertainty-aware length of stay prediction in multi-hospital settings. *Scientific Reports*, 2026. doi: 10.1038/s41598-026-37450-w.

Ali Baheri and Marzieh Amiri Shahbazi. Conformal prediction across scales: Finite-sample coverage with hierarchical efficiency. *Results in Applied Mathematics*, 26:100589, 2025. doi: 10.1016/j.rinam.2025.100589.

Rina Foygel Barber, Emmanuel J. Candès, Aaditya Ramdas, and Ryan J. Tibshirani. Conformal prediction beyond exchangeability. *Annals of Statistics*, 51(2):816–845, 2023. doi: 10.1214/23-AOS2276.

P. Thomas Fletcher. Geodesic regression and the theory of least squares on Riemannian manifolds. *International Journal of Computer Vision*, 105(2):171–185, 2013. doi: 10.1007/s11263-012-0591-y.

Alexander Kuleshov, Alexander Bernstein, and Evgeny Burnaev. Conformal prediction in manifold learning. In *Proceedings of the Seventh Workshop on Conformal and Probabilistic Prediction and Applications*, volume 91 of *Proceedings of Machine Learning Research*, pp. 234–253. PMLR, 2018.

Jing Lei, Max G’Sell, Alessandro Rinaldo, Ryan J. Tibshirani, and Larry Wasserman. Distribution-free predictive inference for regression. *Journal of the American Statistical Association*, 113(523): 1094–1111, 2018. doi: 10.1080/01621459.2017.1307116.

Lizhen Lin, Brian St. Thomas, Hongtu Zhu, and David B. Dunson. Extrinsic local regression on manifold-valued data. *Journal of the American Statistical Association*, 112(519):1261–1273, 2017. doi: 10.1080/01621459.2016.1208615.

Soundouss Messoudi, Sébastien Destercke, and Sylvain Rousseau. Copula-based conformal prediction for multi-target regression. *Pattern Recognition*, 120:108101, 2021. doi: 10.1016/j.patcog.2021.108101.

Soundouss Messoudi, Sébastien Destercke, and Sylvain Rousseau. Ellipsoidal conformal inference for multi-target regression. In *Proceedings of the Eleventh Symposium on Conformal and Probabilistic Prediction with Applications*, volume 179 of *Proceedings of Machine Learning Research*, pp. 294–306. PMLR, 2022.

David Millard, Lars Lindemann, and Ali Baheri. Split conformal prediction in the function space with neural operators. *arXiv preprint arXiv:2509.04623*, 2025.

Valentin Peretroukhin, Matthew Giamou, David M. Rosen, W. Nicholas Greene, Nicholas Roy, and Jonathan Kelly. A smooth representation of belief over $SO(3)$ for deep rotation learning with uncertainty. In *Proceedings of Robotics: Science and Systems*, 2020. doi: 10.15607/RSS.2020.XVI.007.

Alexander Petersen and Hans-Georg Müller. Fréchet regression for random objects with Euclidean predictors. *Annals of Statistics*, 47(2):691–719, 2019. doi: 10.1214/17-AOS1624.

G. N. Ramachandran, C. Ramakrishnan, and V. Sasisekharan. Stereochemistry of polypeptide chain configurations. *Journal of Molecular Biology*, 7(1):95–99, 1963. doi: 10.1016/S0022-2836(63)80023-6.

Yaniv Romano, Evan Patterson, and Emmanuel Candès. Conformalized quantile regression. In *Advances in Neural Information Processing Systems*, volume 32, 2019.

Ryan J. Tibshirani, Rina Foygel Barber, Emmanuel Candès, and Aaditya Ramdas. Conformal prediction under covariate shift. In *Advances in Neural Information Processing Systems*, volume 32, 2019.

Vladimir Vovk, Alex Gammerman, and Glenn Shafer. *Algorithmic Learning in a Random World*. Springer, 2005. doi: 10.1007/b106715.

Ying Yuan, Hongtu Zhu, Weili Lin, and J. S. Marron. Local polynomial regression for symmetric positive definite matrices. *Journal of the Royal Statistical Society: Series B*, 74(4):697–719, 2012. doi: 10.1111/j.1467-9868.2011.01022.x.